Granular flow in a rapidly rotated system with fixed walls

Eric I. Corwin

James Franck Institute and Department of Physics, The University of Chicago, Chicago, Illinois 60637, USA
(Received 30 July 2007; published 19 March 2008)

The flow properties in a granular system confined by a rapidly rotated bottom surface and fixed walls are investigated. Above sufficiently high rotation rates the system enters a state in which the flow is independent of the driving rate. Further, a nearly constant shear-strain rate is measured throughout the entire system. Optical and particle imaging velocimetry methods are used to measure the surface flows, and large-scale molecular dynamics simulations are performed to model the flows both at the surface and in the interior of the material. The analysis shows a regime of granular flow in which shear banding is absent.

I. INTRODUCTION

Bulk flows in granular materials are ubiquitous and of great importance [1–5]. The crushing force of an avalanche, the transport of grain through a hopper, the mixing of pharmaceutical powders, and the cracking of oil in gas-fluidized catalyst beds all rely on the unique properties of granular materials under flow. Granular flows have been divided into rapid dilute flows and dense flows. Rapid dilute flows are similar to molecular gases, dominated by two-body collisions [6]. Dense flows are dominated by many-body interactions, occurring when particles have long-lived contacts with many neighbors [7–12]. Dense flows can in turn be divided into two regimes: fast dense flows which are dominated by the inertia of particles and slow dense flows in which inertia is negligible. Inertia will dominate when the kinetic energy of a particle is much greater than the energy needed to move a particle past its neighbor.

Because of their dissipative nature, granular materials will only flow under the application of a continuous input of energy. When shear stresses are applied to granular materials they typically respond by organizing into rigid regions separated by narrow shear bands ∼10 grains in width [7–12]. Recent experiments have revealed that in the right geometry regions of shear can be created with tunable widths which can increase without bound [13–15]. However, all of these experiments have been conducted in the slow dense regime in which inertia is negligible. This paper introduces a system for probing the nature of flows and shear zones that arise when inertia becomes important. The system consists of a fixed cylinder and a rapidly rotated bottom surface. This study investigates, as a function of driving rate and fill height, the resulting flows in granular materials. A method for producing systemwide shear is presented, the nature of which is explored with experimental measurements and simulational observations. Section II gives background on prior work, Sec. III describes the experimental and simulational techniques used in this paper, and Sec. IV discusses the implications of this work and presents conclusions.

II. BACKGROUND

A. Fluids in rotating buckets

Flows inside rotating buckets have long been studied within the context of fluid mechanics. By considering the motion of water as it comes to rest with the rotating frame in a rotating bucket, Isaac Newton found the equivalence between centripetal and gravitational accelerations as well as the difference between relative and absolute motion [16]. More recently, intriguing shear instabilities have been discovered in a rotating bucket experiment modified such that the walls are held fixed and only the bottom surface is allowed to rotate [17,18]. Such a geometry removes the possibility of the liquid coming to rest with respect to a single rotating frame. Instead, it creates an intense shear at the intersection of the fixed walls and the rotating bottom surface. At high rotation rates a change in the topology of the water is observed. Jansson *et al.* observed the formation and deepening of a void in the center of the water in the system. This void then lost axial symmetry and developed up to six lobes as the driving rate was increased [17]. Suzuki *et al.* have explored the aperiodic switching between the symmetric and nonsymmetric surface deformations in the same system as Jansson *et al.* [18].

B. Spinning granular materials

Several experiments have been performed on granular materials using Newton's rotating cylindrical geometry [19–22]. Vavrek and Baxter measured the surface height profile as a function of rotation rate and elapsed time [19]. They found it to depend on the materials internal angle of friction and proposed a theory which assumes that the surface deforms according to the Coulomb yield condition. They predicted that for ever higher rotation rates the surface will approach a slope set by the internal angle of friction (∼36° for their experiments) in contrast to water, which will approach a slope of 90°. Yeung prepared granular systems that were initially heaped in the center. He then rotated them to discover a metastable state as the heaps evolved toward the asymptotic states predicted by Vavrek and Baxter [20]. Yoon *et al.* tilted the system and found kinks appearing at the boundary between an outer region that was stable and solid and an inner region that was unstable and flowing [21].

A modified version of a spinning cylinder experiment consisted of a split bottom cell in which the center of the bottom is able to rotate with respect to the outer edge and outer wall. This has yielded intriguing results on shear in low-inertia granular flows [13–15]. Fenistein *et al.* observed

a velocity profile which was fit by an error function with a width that could grow arbitrarily large and was independent of the size or details of the granular material used [13,14]. Cheng *et al.* [15] extended this work with particle tracking, MRI imaging, and simulations to measure the internal flows. They observed that radial and axial shear profiles are qualitatively different. While the radial extent is wide and increases with height, the axial width remains narrow and fixed like a traditional shear band.

In order to study the response of granular materials in a regime where inertial effects become important I created a system inspired by the split bottom couette geometry with no central walls as used by Refs. [13–15]. Inertial effects become important in such an apparatus when the centripetal force on a grain due to the rotation of the bottom surface becomes comparable to the gravitational and hydrostatic forces on a grain. However, without modification a split bottom cell is an unsuitable device for exploring flow behavior at high speeds when the system height is small for obvious reasons. For short fill heights if the center of the cell is spun, then the granular material will be ejected from the spinning plate and come to rest on the fixed outer edge of the bottom surface. Likewise, for short fill heights, if the outer region is spun, then the granular material in contact with the outer edge will rapidly come to rest with respect to the rotating frame of the outer wall and bottom surface while the material in the center will remain at rest with respect to the fixed central bottom surface. The only geometry which will allow us to ensure the presence of continuous shear at high rotation rates for all fill heights is one in which the outer cylinder is fixed and the entire bottom surface is rotated. In such a geometry the granular material is driven by the rotation of the bottom surface toward the source of shear at the interface between the rotating bottom surface and the fixed walls.

III. METHODS

A. Experiment

A schematic of the experimental apparatus is shown in Fig. 1. The experimental cell consists of a stationary, removable acrylic cylinder ($R=95$ mm) at the bottom of which a thick acrylic disk is rotated by a high-speed electric motor. A smaller cylinder ($R=35$ mm) may be fitted over the rotating disk to observe any dependencies on container size. Since the rotor must be capable of spinning at high velocity and withstanding the possible uneven loading of the granular material, it is securely mounted onto a 1-in.-diam steel driveshaft held in place by two high-speed bearings separated by a distance of 11.5 in. The vertical wobble of the disk is measured to be less than 250 μm at $r=95$ mm. The driveshaft is spun by a timing belt attached to a 1/2 hp dc motor. The disk can be spun at frequencies f from 0.25 Hz to 46 Hz. The frequency is controlled by a digital feedback loop implemented in LabView software. The speed of the disk is measured by a precision optical encoder (U.S. Digital) with a resolution of ±0.01 Hz. The cell is loaded with a measured mass m of monodisperse spherical soda lime glass beads (Mo-Sci. Corp) of diameter $d=5.0\pm0.05$ mm and mass $m=0.16\pm0.01\times10^{-3}$ kg or diameter $d=1.0\pm0.05$ mm and
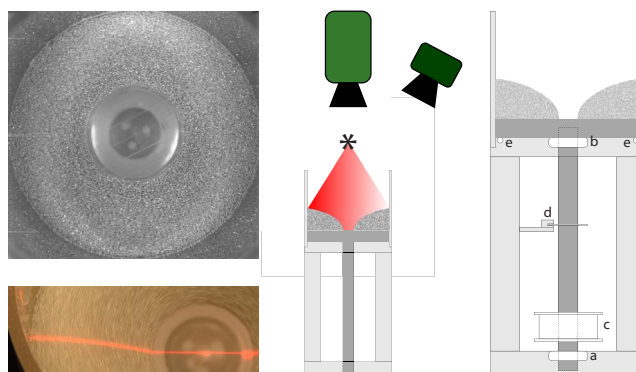

FIG. 1. (Color online) Left-hand side: sample data images of 1-mm beads in a 95-mm system driven at $f=10$ Hz. Above: high-speed video image from directly above. Successive frames are used to compute velocity field using PIV analysis. Below: high-resolution still image taken of laser sheet illuminating surface. This image is taken at an oblique angle to measure the surface height profile. Center: schematic of experimental setup plus data-taking apparatus showing the experimental cell illuminated by a laser sheet and imaged by either a high-speed digital video camera or a high-resolution digital still camera. Right-hand side: diagram of the rapidly rotated system with fixed walls. A 1-in.-diam, 12.5-in.-long steel driveshaft is press fit into two 2-in. high-speed steel bearings (a),(b). Rotation is provided by a timing belt sprocket (c). The rate of rotation is measured by a 2-in.-diam, 100-mark-per-revolution optical encoder (d). The rotor is affixed to the driveshaft and slides smoothly on a 7-in.-diam, 0,25-in. Teflon o-ring (e).

mass $m=0.002\pm0.0005\times10^{-3}$ kg. The approximate fill height H is calculated from the measured fill mass. The top surface of the rotating disk and inner surface of the stationary cylinder can be covered with hard plastic delrin or various grades of sandpaper to change the coefficient of friction. The spinning disk mates with the cylinders of either size with a clearance of less than 250 μm, ensuring that beads cannot get jammed in the gap.

Both the surface height profile of the beads and the surface velocities are measured in the experiments. The surface height profile is detected using a thin laser sheet mounted directly above the center of the cell, spreading across the diameter of the cell (Fig. 1). The scattering of the laser sheet at the line of intersection between the laser sheet and the flowing beads is imaged by a Nikon D70s digital camera at an oblique angle to reveal the surface height profile. To minimize parallax errors the camera is positioned at a distance of 2.25 m and an angle of 8° from vertical and uses a 300-mm zoom lens. This results in a horizontal resolution of 35 μm/pixel and a vertical resolution of 300 μm/pixel. The time-averaged height profile is extracted from long exposure digital photographs.

The surface velocity is measured from high-speed digital video recordings. A Phantom V7 camera is positioned directly above the experimental cell, imaging the granular material (Fig. 1). Video is taken at a rate of 8150 frames/s, an exposure of 30 μs, and a resolution of 608×600 pixels for a period of 1000 frames. The azimuthal and radial components of the surface flow velocity are calculated from the recorded frames using particle imaging velocimetry (PIV)

techniques with the software package GPIV [24]. PIV measures the motion of a small section of an image between neighboring frames. In this paper all PIV measurements were taken between frames separated by 245 μs. Velocities are then averaged over 1000 frames.

B. Simulational

In the system described, experimental techniques only allow observation and measurement of flows at the surface of the granular material. Simulations are employed to peer beneath the surface and more fully understand the resulting flows. Simulations are done using the Large-scale Atomic/Molecular Massively Parallel Simulator (LAMMPS) [23], but modified to reproduce the shearing geometry of the experiments. Spherical grains are used which interact through Hertzian contact forces and tangential frictional forces. The material parameters used to model the spheres are the normal stiffness $k_n = 2 \times 10^4 \ mg/d$, tangential stiffness $k_t = 2/7k_n$, normal and tangential viscous damping coefficients $\gamma_n = 500\sqrt{(g/d)}$ and $\gamma_t = 0$, and the particle and wall coefficients of friction $\mu = 0.5$, where d and m are the diameter and mass of spheres and g is the acceleration due to gravity. The coefficients of damping and friction are approximately equal to those in the experimental system. For computational reasons the stiffnesses must be chosen significantly lower than those in the experimental system. Although an exhaustive search of the phase space of material parameters was not performed, I observed that changing the stiffnesses by an order of magnitude, the damping coefficients by an order of magnitude, and the coefficients of friction between 0.25 and 0.75 neither qualitatively nor quantitatively altered the results of these simulations. Dimensions for the simulated cell match those of the experiments. Simulations are done for 5-mm grains in both the $R = 35$ mm and $R = 95$ mm geometries and for 1-mm grains in the $R = 35$ mm geometry. Simulations are done on systems ranging from 150 up to 50 000 particles.

The initial conditions for the simulations are created by pouring the grains into the cell and allowing them to settle for a simulated period of 10 s. The rotation of the bottom surface is then turned on and the simulation allowed to run for a simulated period of 10 s during which a steady state is achieved, after which the position and velocity are recorded for each particle as a function of simulated time.

IV. RESULTS

A. Height profiles

The radial height profile $z(r)$ is measured as a function of rotation rate f (Fig. 2). For small rotation rates a gentle depression develops in the center of the system, similar to that seen in prior studies of rotated granular or fluid systems [17–22]. As the rotation rate is increased, characteristically different behavior is found for short filling heights ($H < R$) and tall filling heights ($H > R$). Systems with short filling heights undergo a change in topology as the rate of rotation is increased past a threshold frequency f_o. At that frequency, the height at the center drops to zero and a hole opens up in the center of the system, through which the rotor surface is
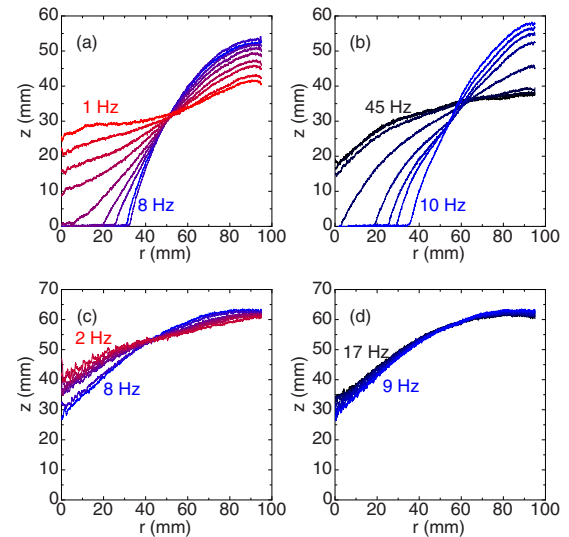

FIG. 2. (Color online) Height as a function of radius for $H \sim 45$ mm or 1.500 kg (a),(b) and $H \sim 85$ mm or 2.500 kg (c),(d) of 1-mm beads in a 95-mm system. (a) Height profile for driving frequencies $f = 1.0, 1.5, 2.0, 2.5, 3.0, 3.5, 4.0, 6.0, 8.0, 10.0$ Hz. At low speeds the surface of the pack is relatively flat. As f is increased, the surface becomes steeper until a hole in the center opens and grows wider. (b) Height profile for $f = 10.0, 15.0, 20.0, 25.0, 30.0, 35.0, 40.0, 45.0$ Hz. As f is increased above ~ 10 Hz, the hole closes and the surface becomes less steep. (c) Height profile for $f = 2.0, 2.5, 3.0, 3.5, 4.0, 6.0, 8.0$ Hz. As f is increased, the surface becomes slightly steeper until 8 Hz. (d) Height profile for $f = 9.0, 10.0, 11.0, 12.0, 13.0, 14.0, 15.0, 16.0, 17.0$ Hz. As f is increased, the surface becomes slightly flatter.

visible. The curvature of the profile also changes markedly, from convex up to convex down. At extremely high rotation rates a second threshold frequency is observed, f_c, above which this topological transition is reversed, the hole closes up, and the surface returns to a profile with a gentle dip in its center. Figure 3 shows a plot of f_o as a function of fill height. The threshold frequency for opening a hole increases rapidly and appears to diverge for some fill height less than R. This suggests that it is impossible to open a hole in a pack of height H greater than the divergence. Indeed, no such topological transition is seen in tall systems.
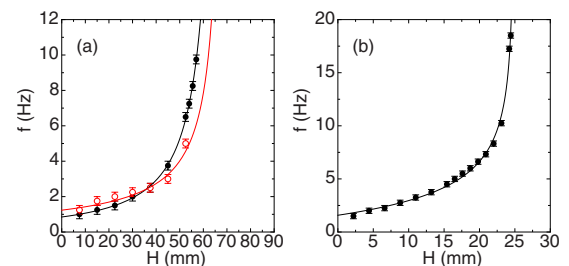

FIG. 3. (Color online) Plot of the threshold frequency of the hole opening, f_o, as a function of the height of beads added, H. (a) 95-mm system. Solid circles correspond to 1-mm grains, and open circles correspond 5-mm grains. (b) 35-mm system. Solid circles correspond to 1-mm grains. Solid lines are guides to the eye.
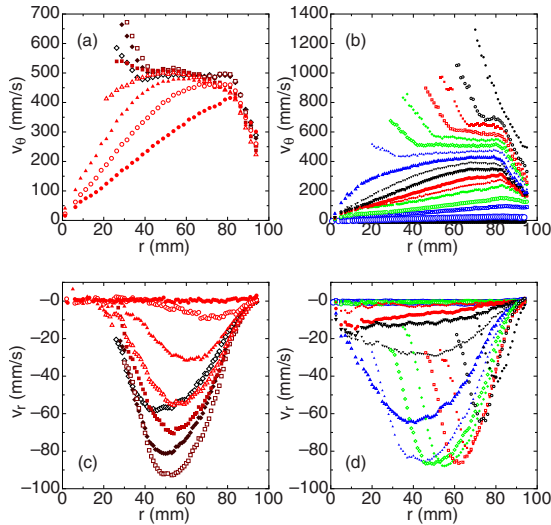
FIG. 4. (Color online) Surface flows for packs of 1-mm beads in $R=95$ mm system. (a) Azimuthal surface velocity v_θ on a $H \sim 45$ mm ($m=1.500$ kg) pack at multiple driving rates $f=1$ Hz (solid circles), 2 Hz (open circles), 3 Hz (solid triangles), 4 Hz (open triangles), 5 Hz (solid squares), 10 Hz (open squares), 20 Hz (solid diamonds), and 30 Hz (open diamonds). (b) v_θ as a function of radius at a driving rate of 10 Hz for multiple fill amounts. The shortest pack is filled with $H \sim 7.5$ mm ($m=0.250$ kg) of beads and plotted as solid circles. Successively taller packs have successively lower values of v_θ and are shown in increments of 7.5 mm up to $H \sim 150$ mm ($m=5.000$ kg). (c) Radial surface velocity v_r on a 1.500-kg ($H \sim 45$ mm) pack at multiple driving rates for the same parameters as in (a). (d) v_r as a function of radius at a driving rate of 10 Hz for multiple fill amounts using the same parameters as in (b).

B. Surface velocity, shear profile

Figure 4 shows the azimuthal (v_θ) and radial (v_r) surface velocities as a function of radius for multiple values of f and H as measured in the $R=95$ mm system with 1-mm beads. Figure 4(a) shows the effect of increasing the driving rate f on v_θ for a pack composed of 1.500 kg of beads (~ 45 mm high at rest). Below $f \sim 2$ Hz the surface azimuthal velocity increases linearly with fixed angular velocity approximately equal to the driving rate, revealing that the beads are rotating as a bulk with minimal slip between the driving rotor and the top surface. At these low frequencies, however, there exists a small region of shear between the pack and the fixed outer walls as evidenced by the dramatic falloff in v_θ close to the outer wall.

As the driving rate is increased toward $f_o \sim 4$ Hz, v_θ reveals significant slip occurring between the top surface and the driving rotor. The very center of the pack still rotates with fixed angular velocity, although now significantly slower than f. There is a broad region from $r \sim 30$ mm to $r \sim 80$ over which v_θ flattens out to a constant velocity of $v_\theta \sim 450$ mm/s, implying a broad region of shear.

Above f_o is a rate-independent regime up to the highest frequencies measured in which the flow is decoupled from the driving rate. Figure 4(b) shows the effect of increased fill

height on v_θ for driving rates in the rate-independent regime ($f=10$ Hz). As the amount of material is increased, the region of constant velocity increases and the value of v_θ decreases. For packs taller than the maximum height for which a hole can open (2.000 kg or $H \sim 60$ mm) there is no longer a region of constant velocity. Instead, the trend is toward a rate-independent bulk rotation at an angular velocity which drops with increased pack height.

Figure 4(c) shows effect of increased f on the radial component of velocity v_r for the same pack as in Fig. 4(a). The data show that, for $f=1$ Hz, $v_r=0$ at all radii, indicating that there is no net flow on the surface into or out of the center. As f is increased, an influx of beads toward the center is observed (v_r is negative) with a characteristic form: the magnitude of v_r is zero at the outer wall and grows to a maximum before falling off to zero again as the center is approached. Taken in conjunction with the data on v_θ this means that individual grains spiral along the top surface from the outer edge of the system into the center. v_r grows with larger f, and the peak moves toward the center until a maximum v_r is observed at $f=10$ Hz. For driving rates higher than this the maximum value of v_r drops and the peak continues to move toward the center. The effects of increased fill height on v_r in the regime in which v_θ is rate independent are detailed in Fig. 4(d). Starting with the shortest systems, as the height is increased, v_r shows evidence of faster flows into the center with the peak position moving closer to the center. For systems taller than the maximum height at which a hole will open v_r begins to decrease while the peak position continues to move toward the center.

For rotational systems the shear-strain rate for velocities in the azimuthal direction changing as a function of radius $\dot{\gamma}_{\theta r}$ is defined such that bulk rotation with a fixed angular velocity has zero shear-strain rate. Further, since the system has rotational symmetry and there is no variation of v_r with respect to θ, there will be no $dv_r/d\theta$ term. Thus, $\dot{\gamma}_{\theta r}$ is defined as the difference between the local angular velocity and the local slope of v_θ versus r:

$$\dot{\gamma}_{\theta r} = \frac{v_\theta}{r} - \frac{dv_\theta}{dr}. \tag{1}$$

The shear-strain rate $\dot{\gamma}_{\theta,r}$ is calculated from the velocity data by taking a numerical derivative. The data in Fig. 4(c) lead to the surprising observation that for 1-mm beads in the 95-mm system a shear field of nearly constant magnitude is present over a width of at least 60 bead diameters (Fig. 5).

C. Simulation comparison to observables

In order to calibrate the simulation and ensure that it is giving meaningful results for experimentally inaccessible regions of the system the simulation must first match the experimentally accessible data set for surface flows. To eliminate any systematic errors in the comparison of the surface velocity profiles, the simulated data are graphically rendered as moving spheres into each frame of a simulated high-speed data set using the same frame rate, camera location, and zoom as in the experimental data. The same PIV analysis
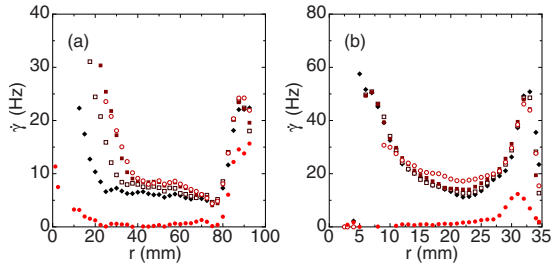
FIG. 5. (Color online) Shear-strain rate $\dot{\gamma}_{\theta,r}$ calculated from the surface azimuthal velocity as a function of radius. (a) Pack consisting of $H \sim 52.5$ mm ($m = 1.750$ kg) of 1-mm grains in a 95-mm system. $\dot{\gamma}_{\theta,r}$ at $f = 1$ (solid circles), 10 (open circles), 20 (solid squares), 30 (open squares), and 40 Hz (solid diamonds). (b) Pack consisting of $H \sim 22$ mm ($m = 0.100$ kg) of 1-mm grains in a 35-mm system. $\dot{\gamma}_{\theta,r}$ at $f = 1$ (solid circles), 10 (open circles), 20 (solid squares), 30 (open squares), and 40 Hz (solid diamonds).

routines as used for the experimental data are applied to this simulated high-speed video (Fig. 6). Figure 7 shows the excellent agreement between surface velocity profiles obtained from simulation and experiment.

D. Simulation azimuthal velocity

Figure 8 reveals that the experimentally observed broad shear is not unique to the surface of the flowing pack, but rather is present throughout the entirety of the system. The flow can be divided into azimuthal (v_θ), radial (v_r), and vertical (v_z) components. Beginning with just the azimuthal components, I can obtain the shear-strain rate in both the $\hat{r}$ and $\hat{z}$ directions. The velocity profiles and shear-strain rate profile in the $\hat{r}$ direction at all heights look qualitatively similar to those measured on the surface [Fig. 8(a)]. The very bottom of the system comes closest to rotating as a bulk with a fixed angular velocity, yet still experiences significant shear-strain rates throughout. However, at larger vertical positions z the trend is toward a fixed velocity v_θ, which decreases with height.
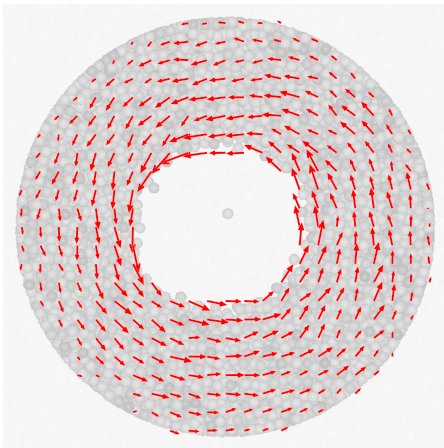

FIG. 6. (Color online) Simulation velocity field superimposed onto rendered simulated data.
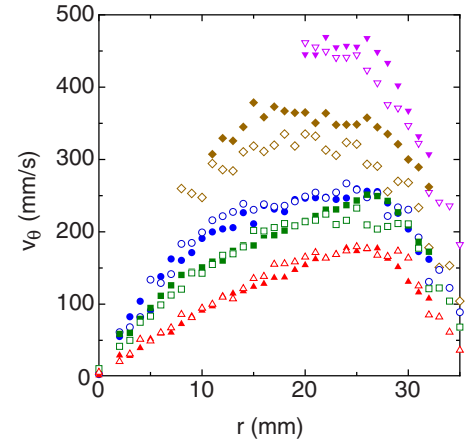

FIG. 7. (Color online) Comparison between surface velocity profiles obtained from experimental (solid symbols) and simulational (open symbols) data on 5-mm beads in a 35-mm system. Data presented for fill heights $H \sim 5.5$ (down triangles), 11 (diamonds), 16.5 (circles), 22 (squares), and 27.5 mm (up triangles).

For systems short enough to open a hole, looking in the $\hat{z}$ direction reveals yet another surprise. At every radius r, v_θ falls off with the logarithm of z, the height as measured from the bottom surface, and is well fit by
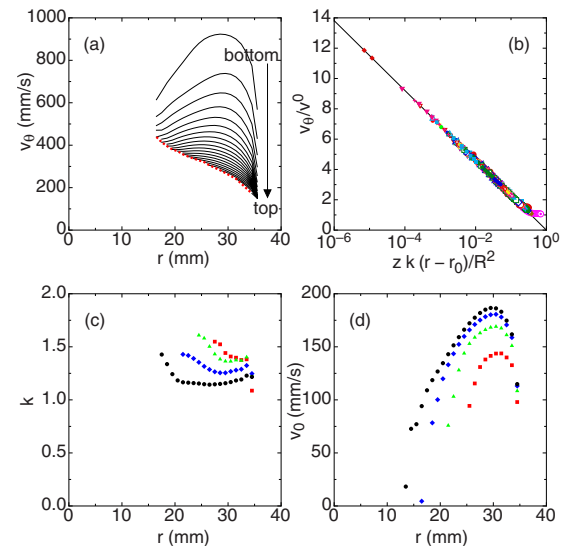

FIG. 8. (Color online) v_θ measured in a simulation of 1-mm beads in an $R = 35$ mm system driven at $f = 10$ Hz. (a) v_θ as a function of r at heights ranging from $z = .5$ mm to 20.5 mm (black lines) for a 50 000 bead simulation (equivalent to 0.100 kg). The thick red line is the velocity at the top surface as a function of radius. (b) v_θ as a function of z scaled onto a single logarithmic curve collapsing data from 12 500 bead, 25 000 bead, 37 500 bead, and 50 000 bead simulations. (c) The dimensionless fit parameter k as a function of r for 12 500 bead (squares), 25 000 bead (triangles), 37 500 bead (diamonds), and 50 000 bead (circles) simulations. (d) The fit parameter v^0 as a function of r plotted with the same symbols as in (c).
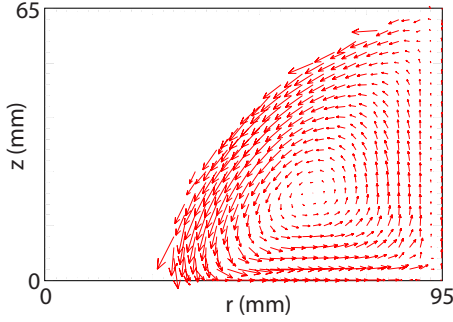
FIG. 9. (Color online) Averaged velocities observed in simulation of 5-mm beads in a 95-mm system. The intensity plot shows the azimuthal velocity v_θ as a function of position. The vector field shows (v_r, v_z) as a function of position revealing the presence of a convection roll.

$$v_\theta(r,z) = v^0(r)\ln\left(\frac{R^2}{k(r-r_0)z}\right), \qquad (2)$$

where v^0 is the fit parameter with units of velocity, k is a dimensionless fit parameter of order 1, and r_0 is the radius of the hole. All v_θ can be collapsed onto a single master curve by plotting v_θ/v^0 versus $zk(r-r_0)/R^2$. The fitting parameters $v^0(r)$ and $k(r)$ are shown in Figs. 8(c) and 8(d).

The shear-strain rate for velocities in the azimuthal direction changing as a function of height, $\dot{\gamma}_{\theta z}$, is defined as

$$\dot{\gamma}_{\theta z} = \frac{dv_\theta}{dz}. \qquad (3)$$

Thus, using the fitting form of Eq. (2) and the fit parameters in Fig. 8, I find that the magnitude of the vertical shear-strain rate for flow in the azimuthal direction falls off as the inverse of height, $\dot{\gamma}_{\theta,z}(r,z) = v^0(r)/z$. The slip between the bottom surface and the top surface is spread throughout the pack, just as I found for the slip due to the outer walls by measuring $\dot{\gamma}_{\theta,r}$.

E. Convective flow

Measurements of v_r along the top surface show beads spiraling into the center of the system. Simulations reveal that this is due to a systemwide convective flow (Fig. 9). Beads at the bottom surface are dragged along by the rotor and rotated with the highest v_θ in the system. As the beads are pushed outwards, they push the beads in front of them toward the wall and then up the side wall. The side wall decelerates v_θ until the beads reach the top surface and flow back down toward the center, where the convective roll begins anew. With the exception of the center line of the convective roll the velocity field reveals that there are no "dead zones" in the pack; every bead is involved in the convective roll. Further, the convective roll does not rotate as a bulk, revealing the presence of additional shearing in the r and z directions.

Figure 10(a) shows the dependence of $\bar{v}_\theta$, the average value of v_θ throughout the system, on the driving rate f. As f is increased, $\bar{v}_\theta$ converges exponentially to the asymptotic
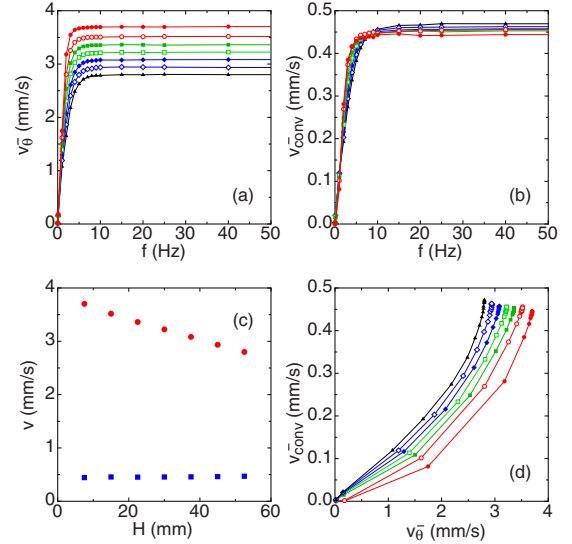

FIG. 10. (Color online) (a) Plot of $\bar{v}_\theta$ as a function of f for 5-mm beads in a 95-mm system filled with $H \sim 7.5$ (solid circles), 15.0 (open circles), 22.5 (solid squares), 30.0 (open squares), 37.5 (solid diamonds), 45.0 (open diamonds), and 52.5 mm (solid triangles). (b) Plot of $\bar{v}_{conv}$ as a function of f for the same parameters as in (a). (c) Plot of asymptotic value of $\bar{v}_\theta$ (circles) and $\bar{v}_{conv}$ (squares). (d) Plot of $\bar{v}_\theta$ versus $\bar{v}_{conv}$ for the same parameters as in a as f is varied from 0.01 Hz to 400 Hz.

value which it achieves in the rate-independent regime. The average velocity of the convection roll can be analyzed in a similar way by examining the average velocity of convection $\bar{v}_{conv}$, which is the average of $\sqrt{v_r^2 + v_z^2}$ throughout the system. Figure 10(b) shows that v_{conv} also converges exponentially to an asymptotic value in the rate-independent regime. Figure 10(c) shows the trend of the asymptotic values of $\bar{v}_\theta$ and $\bar{v}_{conv}$ as a function of system height. $\bar{v}_\theta$ decreases linearly with increased system height while $\bar{v}_{conv}$ increases very gently. If these trends were to continue $\bar{v}_\theta$ would be equal to $\bar{v}_{conv}$ at $H \sim 160$. The relationship between $\bar{v}_\theta$ and $\bar{v}_{conv}$ is shown in Fig. 10(d).

V. DISCUSSION AND CONCLUSION

I have presented comprehensive measurements of the surface height profile, v_θ, v_r, and v_z on the surface and in the bulk of a rapidly rotated system with fixed walls as a function of driving frequency f, radius R, and fill height H for multiple bead sizes.

The existence, and rate independence, of a region of constant velocity v_θ as revealed in both experiments (Fig. 4) and simulations (Fig. 7) appears to be a fundamental property of granular materials in this geometry. The mechanism by which a constant velocity v_θ is created independently of the driving frequency can be understood with a simple model. Consider a parcel of material in contact with both the rapidly spinning rotor and the fixed wall. The material is acted upon through frictional forces by both the rotor and the wall. In the regime in which the rotor is spinning rapidly enough that the parcel is always moving slower than the rotor, the rotor

will accelerate the parcel with an azimuthal force equal to $\mu m g$, where μ is the coefficient of friction between the rotor or wall and the material, and m is the mass of the parcel. The wall will in turn decelerate the parcel with a force equal to $\mu m v_\theta^2 / R$. By equating these two competing forces, I find that the parcel will travel with a fixed velocity of $v_\theta^* = \sqrt{gR}$. Since the region in which beads are in contact with both the rotor and the wall is the primary source of shear in the system, the velocity set there must control the velocities throughout the system. Thus, in order to drive the system into the rate-independent regime the rotor must spin with $f^* > v_\theta^* / 2\pi R$. For the 95-mm system $f^* = 4.1$ Hz and for the 35-mm system $f^* = 6.7$ Hz, in rough agreement with the data presented in Fig. 4, which show $3 < f^* < 5$ Hz for the $R = 95$ mm system and $6 < f^* < 8$ Hz for the $R = 35$ mm system (data not shown here). While this model is only strictly true for a single parcel, it is intriguing to note that it accurately predicts the azimuthal velocity of grains near the interface between the rotor and the wall (Fig. 8).

It can be shown that rate-independent flows for which $f > f^*$ must necessarily be in the fast dense flow regime. A bead participating in the rate-independent flow will have a kinetic energy on the order of $\sim m(v_\theta^*)^2$. The force experienced by a bead will be a sum of both the gravitational and centripetal force. In the rate-independent regime the centripetal force is $\sim (v_\theta^*)^2 / R$ which, by the argument given above, is approximately equal to the gravitational force. Thus, the energy to displace a particle against both the gravitational and centripetal forces is on the order of $\sim mgd$. The ratio between these energies is $\sim R/d$. Therefore, any system that is more than a few bead diameters in radius will be firmly in the fast dense flow regime.

In the regime in which the velocity profile is independent of f, observations of $v_\theta(z)$ reveal pervasive vertical shear (Fig. 8). Further, in this regime, the existence of a region of constant velocity v_θ, independent of radius r, gives rise, through Eq. (1), to a broad region of radial shear across the system. Taken together, these pervasive shears stand in sharp contrast to both traditional narrow shear banding [7–12] and wide shear bands fit by error functions [13–15].

The relationship between $\bar{v}_\theta$ and $\bar{v}_{conv}$ evident in Fig. 10 illuminates the nature of the relationship between the azimuthal flow and the convective flow. Both $\bar{v}_\theta$ and $\bar{v}_{conv}$ tend toward zero as the drive rate f is lowered to zero. The data in Fig. 10(d) show $\bar{v}_{conv}$ as a function of $\bar{v}_\theta$ approaching zero with nonzero slope. Thus, even at small f the convective flow is still present in proportion to the azimuthal flow. If the convective flow were a secondary flow, formed in response to the azimuthal flow, its ratio to the azimuthal flow would

disappear for small enough values of the primary azimuthal flow. That it does not indicates that the convective flow must be a part of the primary flow, inextricably resulting from the mechanical forcing of beads in this geometry even at extremely low f.

While the fluid systems of Refs. [17,18] were notable for the appearance of a breakdown of azimuthal symmetry and the appearance of multilobed structures due to a pronounced shear instability, no such instability was observed in our granular system. I suggest two possible explanations for this disparity. It is possible that the mechanism which is responsible for the decoupling of drive rate from v_θ effectively cuts off the magnitude of the shear below that at which the instability appears. A significantly larger system would have an f^* which grows with $\sqrt{R}$. Perhaps then the shear instability would appear at high f in such a larger system. Alternatively, this could be related to the finite number of beads in the system. The random motion of a finite number of beads may be sufficient to disrupt the collective motion needed for such a shear instability. If I were to go to ever larger systems (or ever smaller grains), perhaps the shear instability would reappear.

An open question remains as to the origin of the surprising collapse of $v_\theta(z)$ seen in Fig. 8. Why the velocity profile should be linear and the resulting shear profile $\dot{\gamma}_{\theta z} \propto 1/z$ is unclear. The form of the collapse in Eq. (2) suggests that this profile is directly tied to the physics determining the opening radius of the hole in the center of the system.

In this paper I have presented an apparatus for achieving a regime in granular flow which generates driving rate-independent flows and systemwide shear. Shear is present between the center of the system and the outer edge as well as between the top of the system and the bottom surface. This geometry may serve as a fruitful starting point for creating more efficient mixing and coating environments. Since there are no static zones and shear is present everywhere, it means that all particles rapidly interact with all other particles. The velocity profiles are insensitive to the grain size and container size, suggesting a scale-invariant and perhaps universal flow field.

[1] S. Savage, Adv. Appl. Mech. **24**, 289 (1984).

[2] H. Jaeger and S. Nagel, Science **255**, 1523 (1992).

[3] B. Ennis, J. Green, and R. Davies, Chem. Eng. Prog. **90**, 32 (1994).

[4] T. Knowlton, J. Carson, G. Klinzing, and W. Yang, Chem. Eng. Prog. **90**, 44 (1994).

[5] D. Scott, Nature (London) **381**, 592 (1996).

[6] J. Jenkins and S. Savage, J. Fluid Mech. **130**, 187 (1983).

[7] J. Duran, *Sands, Powders, and Grains* (Springer, New York, 2000).

[8] L. Bocquet, W. Losert, D. Schalk, T. C. Lubensky, and J. P. Gollub, Phys. Rev. E **65**, 011307 (2001).

[9] R. Behringer, D. Howell, L. Kondic, S. Tennakoon, and C. Veje, Physica D **133**, 1 (1999).

[10] C. T. Veje, D. W. Howell, and R. P. Behringer, Phys. Rev. E **59**, 739 (1999).

[11] D. Mueth, G. Debregeas, G. Karczmar, P. Eng, S. Nagel, and H. Jaeger, Nature (London) **406**, 385 (2000).

[12] M. Toiya, J. Stambaugh, and W. Losert, Phys. Rev. Lett. **93**, 088001 (2004).

[13] D. Fenistein and M. Van Hecke, Nature (London) **425**, 256 (2003).

[14] D. Fenistein, J. W. van de Meent, and M. van Hecke, Phys. Rev. Lett. **92**, 094301 (2004).

[15] X. Cheng, J. B. Lechman, A. Fernandez-Barbero, G. S. Grest, H. M. Jaeger, G. S. Karczmar, M. E. Möbius, and S. R. Nagel, Phys. Rev. Lett. **96**, 038001 (2006).

[16] Isaac Newton, *Scholium to the Definitions in Philosophiae Naturalis Principia Mathematica, Bk. 1 (1689)* (University of California Press, Berkeley, 1934).

[17] T. R. N. Jansson, M. P. Haspang, K. H. Jensen, P. Hersen, and T. Bohr, Phys. Rev. Lett. **96**, 174502 (2006).

[18] T. Suzuki, M. Iima, and Y. Hayase, Phys. Fluids **18**, 101701 (2006).

[19] M. E. Vavrek and G. W. Baxter, Phys. Rev. E **50**, R3353 (1994).

[20] C. Yeung, Phys. Rev. E **57**, 4528 (1998).

[21] S. Yoon, B. H. Eom, J. Lee, and I. Yu, Phys. Rev. Lett. **82**, 4639 (1999).

[22] P. Zamankhan, P. Zamankhan, W. Polashenski, and M. Ghazanfari, Physica D **188**, 40 (2004).

[23] S. Plimpton, J. Comput. Phys. **117**, 1 (1995).

[24] http://gpiv.sourceforge.net/gpiv_home.html